

META-CALIBRATION: DIRECT SELF-CALIBRATION OF BIASES IN SHEAR MEASUREMENT

ERIC M. HUFF¹ AND RACHEL MANDELBAUM²

Draft version August 25, 2016

ABSTRACT

One of the primary limiting sources of systematic uncertainty in forthcoming weak lensing measurements is systematic uncertainty in the quantitative relationship between the distortions due to gravitational lensing and the measurable properties of galaxy images. We present a statistically principled, general solution to this problem. Our technique infers multiplicative shear calibration parameters by modifying the actual survey data to simulate the effects of a known shear. It can be applied to any shear estimation method based on weighted averages of galaxy shape measurements, which includes all methods used to date for shear estimation with real data. Use of the real images mitigates uncertainty due to unknown galaxy morphology, which is a serious concern for calibration of shear estimates based on image simulations. We test our results on simulated images from the GREAT3 challenge, and show that the method eliminates calibration biases for several different shape measurement techniques at the level of precision measurable with the GREAT3 simulations (a few tenths of a percent).

Keywords: cosmology: observations — gravitational lensing: weak — methods: observational

1. INTRODUCTION

Accurate measurement of weak gravitational lensing offers the most direct probe of the dark sector of the universe (e.g., Bartelmann & Schneider 2001; Refregier 2003; Schneider 2006; Hoekstra & Jain 2008; Massey et al. 2010; Weinberg et al. 2013). Weak lensing measurements are thus a core part of the international cosmology program, and a key science driver for several wide-field astronomical imaging cameras and associated surveys – the Kilo Degree Survey³ (de Jong et al. 2015), the Dark Energy Survey (Flaugher 2005), the Hyper-Suprime Camera⁴ (Miyazaki et al. 2012), LSST⁵ (LSST Science Collaborations & LSST Project 2009), Euclid⁶ (Laureijs et al. 2011), and WFIRST⁷ (Spergel et al. 2015).

Despite this investment, the weak lensing community has more work to do in order to ensure that the algorithms for inferring shear are unbiased at the required levels to avoid systematic errors from dominating over the statistical errors. One of the largest such systematic error sources is the *shear calibration bias*, the quantitative relationship between the gravitational lensing signal and its chief observables.

In the weak limit that is most relevant for wide-field cosmology, gravitational lensing signal can be described as a linear transformation $\mathbf{A}\mathbf{x}_{\text{true}} = \mathbf{x}_{\text{obs}}$ between the lensed and unlensed image coordinates, parameterized by two shears (γ_1, γ_2) and a convergence κ

$$\begin{pmatrix} 1 + \kappa + \gamma_1 & \gamma_2 \\ \gamma_2 & 1 + \kappa - \gamma_1 \end{pmatrix} \quad (1)$$

The major observable effect of weak lensing is to per-

turb the measured ellipticities $\mathbf{e} = (e_1, e_2)$ of galaxies. At large separations, these shapes no longer know preferred direction, so the mean \mathbf{e} should vanish over a wide enough field. Weak lensing studies exploit this intrinsic symmetry, and search for spatially coherent anisotropies in the ensemble of observed galaxy shapes arising from lensing distortions produced by foreground matter.

The effects of the shear and convergence on this observable cannot be straightforwardly distinguished, so the fundamental quantity constrained by lensing is the reduced shear

$$g = \frac{\gamma}{1 - \kappa + \gamma}. \quad (2)$$

The responses of individual galaxy images to g vary depending on the choice of ellipticity measure and the intrinsic shape and orientation of each galaxy. Lensing studies rely on ensemble averages of galaxy ellipticities, and the shears are weak enough that this response is usually linear, so it is conventional to define the shear calibration parameters as

$$\mathbf{e} = (1 + m)\mathbf{g} + \mathbf{c} \quad (3)$$

where \mathbf{e} and \mathbf{g} are ensemble-averaged shears and ellipticity measures, respectively. Generally, \mathbf{c} is a result of measurement biases (such as an incomplete correction for the point-spread function) that introduce a preferred direction in the image plane. It can in principle be known or removed with sufficient knowledge of the experiment. m depends in part on the ensemble of (unobserved) galaxy properties, so it is impossible in principle to know exactly *a priori* (though Bernstein & Armstrong 2014 show how to derive this information for their proposed shear estimator from deeper calibration fields).

In practice, nonlinearities generically introduced by the algorithms used for measurement of \mathbf{e} can introduce both multiplicative and additive biases in a manner that interacts with the unknown true ensemble properties of galaxies (Massey et al. 2007b; Zhang & Komatsu 2011), and are very difficult to predict from first principles. For

¹ Jet Propulsion Laboratory, 4800 Oak Grove Drive, Pasadena, CA 91109, USA

² McWilliams Center for Cosmology, Department of Physics, Carnegie Mellon University, Pittsburgh, PA 15213, USA

³ <http://kids.strw.leidenuniv.nl>

⁴ <http://www.naoj.org/Projects/HSC/>

⁵ <http://www.lsst.org/lsst/>

⁶ <http://sci.esa.int/euclid/http://www.euclid-ec.org>

⁷ <http://wfirst.gsfc.nasa.gov>

this reason, the weak lensing community has organized a series of blind measurement challenges, where participants attempted to extract an unknown lensing signal from simulated images. The earliest of these were the first two Shear TESting Programmes (Heymans et al. 2006; Massey et al. 2007a, STEP1, STEP2). The results made two things clear: that lensing measurement algorithms needed to improve, and that shear measurement was sufficiently complex that successive simulation challenges should focus on a subset of the issues.

The next round of simulation challenges – GREAT08, GREAT10, and GREAT3 (Bridle et al. 2009; Kitching et al. 2013; Mandelbaum et al. 2015) – embraced a narrower focus and saw significant performance improvements. They also drove improvements in our understanding of various sources of bias in shear estimation, which is of use in future algorithmic development. The best-performing algorithms from the most recent challenge, GREAT3, reduced m and c to levels approaching those needed for the most ambitious planned lensing measurements, albeit with simulations that did not include all the features of real data.

While this was certainly good news, the narrowed focus of the GREAT challenges necessarily left some of the most important sources of lensing calibration bias untouched. Remaining issues of significant concern include biases resulting from:

- object detection and selection
- deblending
- wavelength-dependent effects
- instrumental defects and nonlinearities
- star-galaxy separation
- non-white pixel noise
- cosmic rays and other image artifacts
- redshift-dependent calibration biases
- shear estimation for low-resolution and/or low signal-to-noise ratio (< 12) galaxies

The impact of these factors depends strongly on the specifics of the experiment. For this reason, shear calibration in current and future experiments relies heavily on simulations designed to match the properties of each experiment (Hildebrandt et al. 2016; Jarvis et al. 2016). Such external simulations are always limited in their realism: they must accurately model everything relevant about the experiment. Showing that a given simulation suite is adequate for calibrating a lensing measurement is a formidable challenge in its own right (c.f. the Ultra Fast Image Generation simulations described in Bergé et al. 2013, or the calibration simulations used for the KiDS weak lensing cosmology in Fenech Conti et al. 2016).

This method outlined in this paper is motivated by the observation that introducing a synthetic shear signal into real data is much easier than building a realistic comprehensive simulation suite. Perturbing the actual data automatically incorporates features present in real images (e.g., image artifacts, selection biases, unusual high-redshift galaxy morphologies) that are otherwise difficult to accurately simulate.

We have implemented this idea, which we call metacalibration, using the public GalSim (Rowe et al. 2015) image simulation package, and designed our algorithm to wrap an arbitrary external shear estimation module. We test our technique on simulated GREAT3 image data, and find that it successfully calibrates older shear estimation methods to a level of accuracy comparable to the best-performing algorithms from the GREAT3 challenge. We also demonstrate that our algorithm can detrend additive biases resulting from incomplete PSF corrections by introducing synthetic PSF ellipticity. We make our metacalibration scripts available for general use.

2. METHOD

There are three layers to the shear calibration method we propose here. The first is the generation of the counterfactual images, and here our proposed procedure here is similar in detail to one proposed in (Kaiser 2000). We use the GalSim package (Rowe et al. 2015) to modify real astronomical images by adding synthetic shear and PSF distortions of known amplitude. These modified images are counterfactuals; they are a model for what would have been observed under (nearly) the same image quality conditions, on the same galaxies, with a different shear. If the measurement process is repeated on the counterfactual images, the result gives an accurate estimate of shear calibration biases.

The second layer is the choice of ellipticity measure. This step is the primary focus of most studies that attempt to address shear calibration biases. Here we are agnostic about the choice of measurement algorithm; as long as the algorithm is sufficiently well-behaved (in a manner we will describe below), the image manipulation step can be used to generate an accurate shear sensitivity.

The final layer is the choice of averaging mechanism. Noise properties of shape measures can vary widely, which entails similar variation in the metacalibration estimates for shear responsivity. For the cases we describe below, an optimal strategy for ensemble averaging produces significant gains over more straightforward averaging schemes.

2.1. Generating a Counterfactual Image

Fortunately, for the weak shears under consideration in most cosmological survey applications, the relationship between the shear and the galaxy shapes (or related observables) is very close to linear, so accurate shear calibration requires only the first derivative of the galaxy properties with respect to the shear. What follows is a method for estimating this derivative directly from the images. Throughout we will assume that the observed image $I(\mathbf{x})$ is equal to the unsmeared galaxy image $G(\mathbf{x})$ convolved with some seeing kernel $P(\mathbf{x})$.

In an ideal world, we would vary the gravitational shear experienced by the image before it is smeared by P , constructing the counterfactual image $I'(\mathbf{x}|\mathbf{g})$:

$$I'(\mathbf{x}|\mathbf{g}) = P * (\hat{\mathbf{s}}_{\mathbf{g}} G) \quad (4)$$

where $\hat{\mathbf{s}}_{\mathbf{g}}$ is the shear operator that produces the reduced shear \mathbf{g} , as in e.g. Bernstein & Jarvis (2002). The shear sensitivity of the image would then be a straightforward numerical derivative of I' with respect to \mathbf{g} , and the shear

sensitivity of an ellipticity measure \mathbf{e} can be got from measurements on multiple \cdot . We can even write down a procedure for producing I' from I if we know P :

$$I'(\mathbf{x}) = P * [\hat{\mathbf{s}}_{\mathbf{g}} (P^{-1} * I)]. \quad (5)$$

The noise in I has finite power on scales where P is small or vanishing. Deconvolution amplifies noise, and because of the shear, this is not cancelled by reconvolution with P . The noise amplification can be mitigated by reconvolving after the shear operation with a new PSF Γ , (instead of P) and constructing Γ so that it suppresses the noise amplification that is produced by the deconvolution operation.

All that is required for this is that (in Fourier space, with the tilde indicating the Fourier transformed quantity) $\|\tilde{\Gamma}(\mathbf{k})\| \geq \|\hat{\mathbf{s}}\tilde{P}(\mathbf{k})\|$ for all \mathbf{k} which can be met without introducing additional PSF anisotropy by choosing $\Gamma(\mathbf{x}) = P((1 + 2|\gamma|)\mathbf{x})$.

Our chosen procedure for producing a sheared counterfactual image is

$$I' = \Gamma \otimes [\hat{\mathbf{s}}_{\mathbf{g}} (P^{-1}I)]. \quad (6)$$

This procedure clearly requires a good model for P , but so do all shear measurements. PSF model errors enter at the same order in measurements on the resulting image that they would in an unmodified image.

Once the counterfactual image $I'(\mathbf{x}|\mathbf{g})$ with $\|\mathbf{g}\| \ll 1$ has been created, the galaxy detection and shear measurement pipeline should be rerun. This provides a measure of the shear sensitivity – not for the original image, but for an image with the PSF Γ . This requires that the full measurement – not just the sensitivity analysis – be run on an additional counterfactual image $I'(\mathbf{x}|\mathbf{g} = 0)$, so that the numerical derivative $\frac{\partial I'}{\partial \mathbf{g}}$ is well-defined.

This procedure introduces correlated, anisotropic noise, which can produce a systematic multiplicative shear bias. If the noise properties of the initial image are known, the noise anisotropy can be removed with additional anisotropic noise. As we describe below, we have not found noise isotropization to be a necessary step for the images that we used for testing. These have an effective S/N limit of ~ 12 . The forthcoming Sheldon et al. (2016) will investigate the effects of correlated noise at lower signal-to-noise ratios, and describe effective mitigation procedures.

Metacalibration can be used to mitigate other systematics as well. Even those measurement methods with the highest scores in the GREAT3 lensing challenge were unable to completely remove the effects of PSF ellipticity on the inferred shear. We can introduce an artificial PSF anisotropy by replace Γ with a PSF containing the desired synthetic distortion. We show below that reconstructing images with added PSF ellipticity, rather than added shear, allows us to de-trend some of the bias due to of PSF anisotropy. A similar approach could be used to measure calibration biases arising from any effect – signal or systematic error – that can be simulated by perturbing the images as above.

2.2. Shape Measurement Algorithms

Accurate ensemble shears can only be derived from the counterfactual images described above if the shape measurement algorithm is sufficiently well-behaved. Here,

that entails the requirement that the quantity reported by the shape measurement algorithm be linear in the underlying shear in the regime relevant for the measurement.

We test a variety of shape algorithms below that make use of differing definitions of ellipticity. As we are attempting to construct a shear calibration procedure that is agnostic about the choice of estimation algorithm, and which only requires that we use a measured galaxy property with approximately linear sensitivity to shear (called a shape measure), we will use \mathbf{e} below to signify all of the shape measures discussed in this paper, regardless of their precise definition.

2.3. Ensemble Shear Inference

Counterfactual images can be used to derive a per-object shear response for a modified version of the original image, as described above. However, the quantities of interest in Eq. 3 are ensemble responses.

(EMH: It's really not clear when averaging should work, and when it fails why the histogram estimator should work instead. We have precious little theory at this point about when our proposed procedure should be expected to break.)

3. IMPLEMENTATION

3.1. Image Modification

We use GalSim⁸ to manipulate the images and to generate simulations for validation. For each galaxy, we create nine modified images: two for each of the two shear components, two for each of the two PSF ellipticity components, and one for the final measurement using the enlarged PSF Γ (our estimates of the shear and PSF ellipticity response were less noisy when we used a two-sided derivative). We run the provided shape measurement pipeline on each of these images, and the results are used to construct a set of finite difference estimates of calibration and PSF biases.

This sort of image manipulation is trivial to carry out using GalSim; we rely on the rigorous testing of the image convolution, interpolation, and resampling algorithms that the development team performed to enable the GREAT3 shear testing simulations. From the perspective of numerical validation, the tests in section 9 of Rowe et al. (2015) illustrate that GalSim can accurately render sheared images of quite complex galaxy and PSF light profiles with its default settings that control numerical accuracy.

For each galaxy and PSF postage stamp, we first create an `InterpolatedImage` object. This object is deconvolved by the PSF model (including the pixel response). For the shear finite differences, we apply a small shear $\Delta \mathbf{g}$ (typically 1%) to the resulting deconvolved image. The original PSF is dilated by twice the shear distortion to produce Γ , and then re-convolved with the sheared deconvolved image. This reconvolved, sheared image is then passed to the shape measurement routine, along with the image representation of the new, enlarged PSF Γ . For the PSF sensitivity, we follow a similar procedure, but shear the dilated PSF image rather than the deconvolved galaxy image. Finally, we create a recon-

⁸ <https://github.com/GalSim-developers/GalSim>

volved image with no added shear but with the PSF Γ , on which we perform the final shape measurement.

Shape measurements on these images are used to derive shear calibration and PSF biases introduced by the chosen shape measurement method. The shapes measured from the sheared reconvolved images with positive and negative applied shears, \mathbf{e}_+ and \mathbf{e}_- , can be used for a straightforward finite-difference estimate of the multiplicative shear calibration

$$R = \frac{\partial \mathbf{e}}{\partial \mathbf{g}} \quad (7)$$

$$= \frac{\mathbf{e}_+ - \mathbf{e}_-}{2\Delta \mathbf{g}} \quad (8)$$

Additive biases introduced by the shape measurement are related to the sum of these two quantities:

$$\mathbf{c} = \frac{\mathbf{e}_+ + \mathbf{e}_-}{2} - \mathbf{e} \quad (9)$$

and if the shape measurement algorithm does not perfectly remove PSF ellipticity, then the shapes measured from shearing the PSF ($\mathbf{e}_{+, \text{PSF}}$ and $\mathbf{e}_{-, \text{PSF}}$) permit calculation of at least the linear-order residual PSF ellipticity biases:

$$R_{\text{PSF}} = \frac{\mathbf{e}_{+, \text{PSF}} - \mathbf{e}_{-, \text{PSF}}}{2\Delta \mathbf{g}}. \quad (10)$$

The result of this process is a catalog of shear responsiveness, PSF responsiveness, and additive biases for every galaxy. A histogram of these quantities is shown in figure 1. The derived biases and responsiveness are very noisy, so attention must be paid to how inference is performed on the full ensemble of galaxies.

3.2. Shear Estimation Algorithms

Since the metacalibration method can in principle be used to calibrate shears from any shear estimation algorithm derived using an average of per-object shapes, we chose three easily available shear estimation methods, all of which are implemented in GalSim. Two of these methods are traditional shear estimation methods that have somewhat different assumptions but are both based on object moments. One method is not a standard shear estimation method at all: we use linear combinations of the directly observed second moments without any correction for the PSF. In principle, the information about how those respond to shear should be determined by metacalibration to correctly infer the shear. The difference in this case is that instead of providing a small correction to the outputs of a PSF correction method, we rely on metacalibration to do the entirety of the PSF correction, which is a very stringent test that may at least partially violate some of the assumptions about linearity of responses to shear. The three methods are described below.

3.2.1. Regaussianization

Re-Gaussianization (Hirata & Seljak 2003) is a PSF correction method based on the use of the moments of the image and of the PSF to correct for the effects of the PSF on the galaxy shapes. It includes corrections for the non-Gaussianity of the galaxy profile (Bernstein & Jarvis 2002; Hirata & Seljak 2003) and of the PSF (to first order

in the PSF non-Gaussianity). The performance of this algorithm has been extensively studied in real data and simulations (e.g., Mandelbaum et al. 2005, 2012, 2013, 2015). In the remainder of this paper, we

The outputs of the re-Gaussianization algorithm are PSF-corrected “distortions”, which for an object with purely elliptical isophotes with minor-to-major axis ratio q and position angle θ with respect to the x axis in pixel coordinates are defined as

$$(e_1, e_2) = \frac{1 - q^2}{1 + q^2} (\cos 2\theta, \sin 2\theta). \quad (11)$$

As discussed in Bernstein & Jarvis (2002), the response of a distribution of galaxies with some intrinsic distribution of distortions $p(e)$ to a shear depends on the $p(e)$ itself. Conceptually, we can think of an ensemble shear estimator using re-Gaussianization outputs as

$$\hat{g}_j = \frac{\langle e_j \rangle}{d\langle e_j \rangle / dg_j} \quad (12)$$

where the denominator gives the response of the ensemble average distortion to a shear (often called the responsivity). Estimators of this shear responsivity use the observed galaxy $p(e)$ and its moments, and for typical $p(e)$, the denominator is around $1.7\text{--}1.8 \approx 2(1 - e_{\text{RMS}}^2)$ in terms of the per-component RMS distortion.

(RM: We should take the comment from the GREAT3 results paper about the difference between this regaussianization implementation, vs. those used for SDSS science.)

3.2.2. KSB

The KSB method (Kaiser et al. 1995) parametrises galaxies and stars according to their weighted quadrupole moments. The main assumption of the KSB method is that the PSF can be described as a small but highly anisotropic distortion convolved with a large circularly symmetric function. With that assumption, the shear can be recovered to first-order from the observed ellipticity of each galaxy via

$$g = P_g^{-1} \left(e^{\text{obs}} - \frac{P^{\text{sm}}}{P^{\text{sm}*}} e^* \right), \quad (13)$$

where asterisks indicate quantities that should be measured from the PSF model at that galaxy position, P^{sm} is the smear polarisability (see Heymans et al. 2006 for definitions) and P_g is the correction to the shear polarisability that includes the smearing with the isotropic component of the PSF. The ellipticities are constructed from weighted quadrupole moments, and the other quantities involve higher order moments. A circular Gaussian weight of scale length r_g is used, where r_g is galaxy size.

The KSB method returns a per-object estimate of the shears (\hat{g}_1, \hat{g}_2). We can use metacalibration to infer the ensemble shear, removing multiplicative and additive biases that come from averaging the per-object KSB shear estimates.

3.2.3. Linear Moments

As mentioned previously, the third method we use does not involve PSF-corrected galaxy shapes. Instead, we use

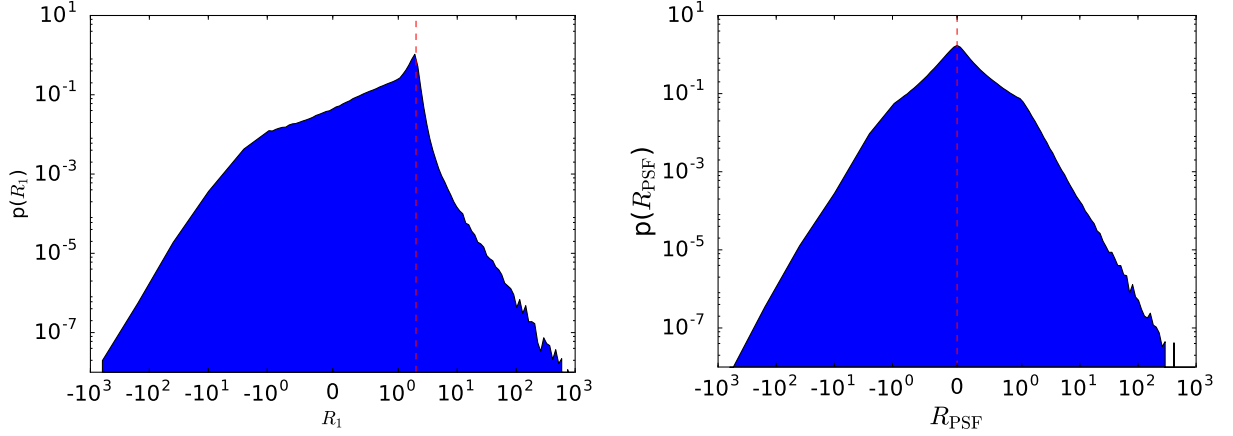


Figure 1. **Left:** Normalized distribution of meta-calibration shear responsivities from regaussianization, on the Control-Ground-Constraint branch of the GREAT3 simulations. **Right:** Distribution of meta-calibration PSF ellipticity responsivities from regaussianization, on the Control-Ground-Constraint branch of the GREAT3 simulations. A vertical red dashed line is drawn for reference at the expected responsivity for perfectly round objects, $R = 2$, in the left panel.

linear combinations of the second moments of galaxy images. The motivation behind this choice is as follows. One way to estimate the distortion (e_1, e_2) is via combinations of the second moments of the light profile,

$$\langle x_i \rangle = \frac{\int x_i w(\mathbf{x}) I(\mathbf{x}) d^2 \mathbf{x}}{\int w(\mathbf{x}) I(\mathbf{x}) d^2 \mathbf{x}} \quad (14)$$

for $i = 1, 2$,

$$M_{ij} = \frac{\int (x_i - \langle x_i \rangle)(x_j - \langle x_j \rangle) w(\mathbf{x}) I(\mathbf{x}) d^2 \mathbf{x}}{\int w(\mathbf{x}) I(\mathbf{x}) d^2 \mathbf{x}} \quad (15)$$

for $i, j = 1, 2$, and finally

$$e_1 = \frac{M_{11} - M_{22}}{M_{11} + M_{22}}, \quad e_2 = \frac{2M_{12}}{M_{11} + M_{22}}. \quad (16)$$

One source of noise (including noise bias) in traditional moments-based methods is the division of two noisy quantities in Eq. 16, typically followed by further division by other noisy quantities to remove the dilution of the galaxy shape by the PSF. Thus, as a final example of a statistic that we will attempt to use as a calibrated shear estimator with metacalibration, we define the following linear combinations of moments:

$$\hat{M}_i = (M_{11} - M_{22}, 2M_{12}). \quad (17)$$

Clearly these moments are sensitive to a number of nuisance quantities, like the galaxy flux and size, and the PSF size and shape. In principle, metacalibration should be able to nonetheless determine the response of this statistic to shear, $d\hat{M}_i/dg$, and produce a reliable shear estimate, provided that the model for the predominant sources of systematics follows that in Eq. 18. This is a quite stringent test of the metacalibration method, as it is unclear whether that purely linear model will be valid in this case.

3.3. Ensemble Inference

We test the metacalibration procedure on two different shear estimation methods – regaussianization and KSB – each of which is known to have calibration biases that

depend on the S/N , galaxy size and morphology, and so on. For both methods, we use the entire ensemble of measured shapes to build a model of the *unlensed* shape distribution, $p_0(\mathbf{e})$. There is no guarantee that the average shear over the ensemble is actually sufficiently small to allow unbiased inference, however, so we symmetrize this model distribution by averaging it with its reflection about $\mathbf{e} = 0$ (note that the resulting model for the null shape distribution will be somewhat broader than the true distribution of ellipticities at zero shear). The newly symmetrized model unlensed distribution is $p_{0,\text{sym}}$. We assume that the ellipticities in each field transform as

$$e_{\text{meas}} = e_0 + R_{\text{PSF}} e_{\text{PSF}} + Rg + c \quad (18)$$

where e_{meas} is the vector of measured ellipticities, and noisy estimates of the constants R_{PSF} , R , and c have been determined separately for each galaxy, as described above, during the image modification step. This is then used to construct a linear estimator for the ensemble shear, as follows.

If the measured shape distribution $n(\mathbf{e}_{\text{meas}})$ is linear in the shear, then we can write

$$\frac{n(\mathbf{e}_{\text{meas}})}{N_{\text{tot}}} = p_{0,\text{sym}}(\mathbf{e}) + \mathbf{g} \cdot \partial_g p_{0,\text{sym}}(\mathbf{e}) \quad (19)$$

It will be convenient to discretize this distribution into a histogram. If the probability of a galaxy ending up in the i^{th} shape histogram bin is q_i , and each galaxy's shape can be considered an independent draw from some underlying distribution, then the likelihood function for an observed histogram is exactly the multinomial likelihood

$$p(\{N_i\} | \{q_i\}) = \frac{N_{\text{tot}}!}{\prod_i (N_i!)} \prod_j q_j^{N_j} \quad (20)$$

where $N_{\text{tot}} = \sum_i N_i$ is the total number of samples in the histogram. The covariance matrix for the bin amplitudes

of this histogram is

$$\text{cov}(N_i, N_j) = C_{ij} = \begin{cases} q_i(1 - q_i)N_{\text{tot}}, & i = j \\ -q_i q_j N_{\text{tot}}, & i \neq j. \end{cases} \quad (21)$$

To make the notation for what follows less cumbersome, let the normalized histogram be $h_i = N_i/N_{\text{tot}}$, and its first derivative with respect to the shear be $\Delta_h = \partial_g \mathbf{h}_{\text{fid}}$.

Given a measured shape histogram with some unknown shear and a fiducial, unlensed shape histogram, the (component-wise) minimum-variance estimator for g is

$$\hat{g} = \frac{\Delta_h^T C^{-1} (\mathbf{h}_{\text{meas}} - \mathbf{h}_{\text{fid}})}{\Delta_h^T C^{-1} \Delta_h}, \quad (22)$$

with variance

$$\sigma_{\hat{g}}^2 = \frac{1}{\Delta_h^T C^{-1} \Delta_h} \quad (23)$$

This method for shear inference has as its tunable parameter only the histogram binning scheme. Once we have chosen a suitable scheme, we then bin the prior into equal-number bins and calculate its shear derivative using equation 18 by adding a small shear \mathbf{g} using the per-object responses, then rebinning. This provides the inputs for the per-field shear estimation. To carry out the per-field shear estimation, we calculate a shape histogram with these bins for each separate field, and evaluate equations 22 and 23 using the globally-derived Δ_h^T .

If we have a poor model for the unlensed histogram, \mathbf{h}_{fid} , then the results will be biased. We can define a distance between each field and the unlensed model using equation 20, taking the probabilities q_i from the unlensed model and the histogram amplitudes from the current field, after correcting for the estimated shear. If the shear response measured for the unlensed prior is correct, then the performance of the estimator will depend only on the similarity of the model to the measurement field. The likelihood can then be used as an objective criterion for the quality of the inference.

3.4. Relationship to previous implementations

As shown in the GREAT3 results paper (Mandelbaum et al. 2015), an early version of metacalibration was used in the GREAT3 challenge. That implementation differs from the one presented here and released publicly in association with this paper in two important ways: the model for systematics was simpler than the one presented below (in particular, it neglected additive systematics entirely in favor of focusing exclusively on multiplicative systematics) and the method for inferring shears from an ensemble of objects was entirely different. These differences are of sufficient importance that the GREAT3 results (especially the ones for additive systematics) are not relevant to the implementation described here.

4. TESTING FRAMEWORK

We test the performance of our algorithm on simulated image sets. Our baseline simulations are drawn from the GREAT3 simulation suite. We run additional simulations in order to distinguish between potential biases arising separately from the three components of our inference framework.

4.1. Simulated Images

We use the GREAT3 simulation framework as the source of simulated images that we use for testing purposes. For more detail about that simulation framework, see the GREAT3 handbook (Mandelbaum et al. 2014) and results paper (Mandelbaum et al. 2015), or the publicly available software⁹.

In brief, we use simulated “branches” containing 200 “subfields”. Each subfield contains 10^4 galaxies placed on a 100×100 grid; the galaxies in a given subfield all have the same (unknown) shear and the same known PSF. The galaxy population within a subfield follows a distribution of signal-to-noise ratio, size, ellipticity, and morphology based on that in the *Hubble Space Telescope* (HST) COSMOS survey (Koekemoer et al. 2007; Scoville et al. 2007b,a), roughly approximating a galaxy sample with a depth of $I < 25$. To ensure that most methods will be able to measure all galaxies, an effective signal-to-noise cut¹⁰ of $\gtrsim 12$ and a minimal resolution cut was imposed (resulting in different sets of galaxies in subfields that have different-sized PSFs). 90° rotated pairs of galaxies were included, to cancel out shape noise (Massey et al. 2007a). The PSF in the simulations comes from the combination of an optics model from a ground-based telescope, along with a Kolmogorov PSF with a typical ellipticity variance. Thus, the galaxy and PSF properties are non-trivially complicated. The noise is stationary Gaussian noise. The ultimate goal is to estimate the average shear in each subfield in an unbiased way, without any multiplicative bias or correlations with the per-subfield PSF ellipticity.

One important distinction between GREAT3 and the real Universe that we will have to consider is the mean shear. In a real patch of sky comparable to the size of a large survey, the expected mean shear is zero. In GREAT3, while lensing shears g_1 and g_2 are drawn from a distribution with zero mean, the fact that there are only 200 subfields means that effectively only 200 draws from that distribution were made, and that is not enough to have an effective mean shear of zero. Thus, for all of the results below, we will take the averages of the true shears per component as a known quantity instead of doing a fully blind analysis, since the deviation of those quantities from zero is just due to the artificial nature of the simulation design.

We consider two sets of galaxy populations. One comes directly from HST images, and includes a process to remove the HST PSF before shearing (both operations being carried out in Fourier space) and convolving with the final target PSF (Mandelbaum et al. 2012). The other galaxy population consists of simple parametric representations of those HST images. These populations have the same effective distributions of size, ellipticity, and so on, but one includes realistic galaxy morphology while the other only includes such realism as can be captured by the sum of two Sérsic profiles. In the language of GREAT3, we use simulations corresponding to control-ground-constant (describing the parametric galaxy sample), ground-based simulated data, with a constant per-

⁹ <https://github.com/barnabytprowe/great3-public>

¹⁰ This was initially advertised as a cut at 20, however the GREAT3 results paper shows that for a more realistic signal-to-noise estimator, the effective cut is around 12.

subfield shear) and real_galaxy-ground-constant (the realistic galaxy sample), denoted CGC and RGC.

4.2. Simulation Branches

The simplest of our simulation tests was performed on a newly-generated set of simulations that is closely analogous to the GREAT3 CGC branch (parametric galaxy profiles), but with one modification to avoid a problem raised in the results paper (Mandelbaum et al. 2015). There, it was noted that the CGC branch has a number of outlier fields related to unusually large optical PSF aberrations, specifically defocus and trefoil. Thus, our first simulated dataset is designed exactly like CGC but with all aberrations in the optical PSF set to zero, to ensure reasonable consistency of data quality. Note that the atmospheric PSF is still drawn from a distribution of seeing values for each subfield. For this branch, it is not necessary to use a likelihood cut to remove fields with aberrant PSF behavior in defining the null ellipticity distribution, and so we include all branches in our analysis. In the accompanying figures and table, this branch is denoted by “CGC-noaber-regauss”.

The next branch we analyze is similar to the previous one, but with realistic galaxies. This lets us separate the effects of realistic galaxy morphology from the problems inherent in correcting a complex PSF. Just as with the previous branch, is not necessary to use a likelihood cut to remove fields with aberrant PSF behavior in defining the null ellipticity distribution, and so we include all the generated fields in our analysis. The results from this branch are labelled “RGC-noaber-regauss”.

We use the GREAT3 CGC simulation branch as a baseline, and report the performance of metacalibration on this branch for all three of our chosen shape measurement algorithms; our results here are denoted in the accompanying figures and tables with the labels “CGC-regauss”, “CGC-moments”, and “CGC-ksb”, as appropriate. Tests on this branch allow straightforward comparison between the performance of our chosen procedure and the variety of other algorithms tested in the GREAT3 challenge.

We next report results for the GREAT RGC branch, incorporating more realistic galaxy morphologies along with the aberrant PSFs introduced in the CGC branch.

One issue of concern is how to understand outlier fields. In GREAT3, there was a concern that some outliers were due to failure of our model for interpreting the per-object shapes in fields that had large aberrations.

As a way to understand this, we generated a version of RGC that had quite large aberrations that were identical in each field: specifically defocus of 0.5 waves and one component of trefoil of 0.1 wave. An example of a PSF in one subfield is shown in Fig. 4; they do not all look identical, since the atmospheric component was still allowed to vary stochastically according to some seeing distribution. This removes the difficulties in building a null ellipticity distribution, isolating the impact of a complex PSF. The results from this simulation are labelled “RGC-FixedAber-regauss”.

Finally, we investigate the effects of increasing the noise in the images. We re-run the “CGC-regauss” analysis five times, increasing the noise in the initial image each time. The correlated noise produced by the image modification procedure may affect the derived calibra-

tion, and we expect this number of realizations to demonstrate whether correlated noise biases is consistent with some simple signal-to-noise scaling. The results of simply doubling the noise are shown in the summary results figures and table below with the label “CGC-regauss-noisy”.

5. RESULTS

The primary results from our correction procedure are shown in Figures 7 and 8. The calibration biases for individual fields before and after metacalibration for several branches are shown in Figure 2.

In every test we run, metacalibration appreciably reduces the shear calibration bias. For all of the regaussianization tests, the results are consistent with no remaining calibration biases. Metacalibrating KSB results in marginally significant residual calibration bases, and the magnitude of the average multiplicative calibration bias m is reduced relative to its uncorrected value by about an order of magnitude. The moments shapes are also still biased after metacalibration, though here our procedure has suppressed the calibration bias by almost two orders of magnitude; metacalibrated raw moments appear to perform better than uncorrected KSB.

Our PSF detrending scheme reduces the amplitude of residual trends between the PSF ellipticity and the inferred shear, though the reductions in a are less dramatic than those in m . The residual PSF trends for several of the branches are shown in Figure 5. Fields with large PSF ellipticity outliers appear to be driving most of the residual trends. This should perhaps not be surprising, as our assumption that the primary channel by which the PSF affects the inferred shear is the PSF ellipticity is not completely general, and may in general vary with the choice of algorithm or the properties of the PSF.

Figure 3 shows the impact of adding additional noise on the metacalibrated shears. The resulting calibration bias appears to scale as the variance, though at least for the “CGC-regauss” branch we tested here the effects do not become statistically significant until the noise is approximately doubled.

6. APPLICABILITY TO REAL DATA

Several implementation issues need to be solved before this method can be deployed on real survey data. We have made no attempt to deal with the effects of masked pixels or blending, and while it seems clear that our proposed algorithm has the potential to deal with selection biases, we have not demonstrated that capability here. We have also demonstrated the presence of a calibration bias which scales with the variance of the pixel noise, which may be a result of the correlations imposed on the noise field during the construction of the counterfactual image.

In this work, we have attempted to remove PSF systematics by measuring the response of the shape measure to PSF ellipticity. There is no guarantee, however, that the PSF ellipticity is the correct parameter to use for this detrending. In a realistic measurement, it would be best to first determine which modes of PSF variation are most likely to impact the chosen shape measure, and then use the image modification and detrending technique described here to remove those effects in the data.

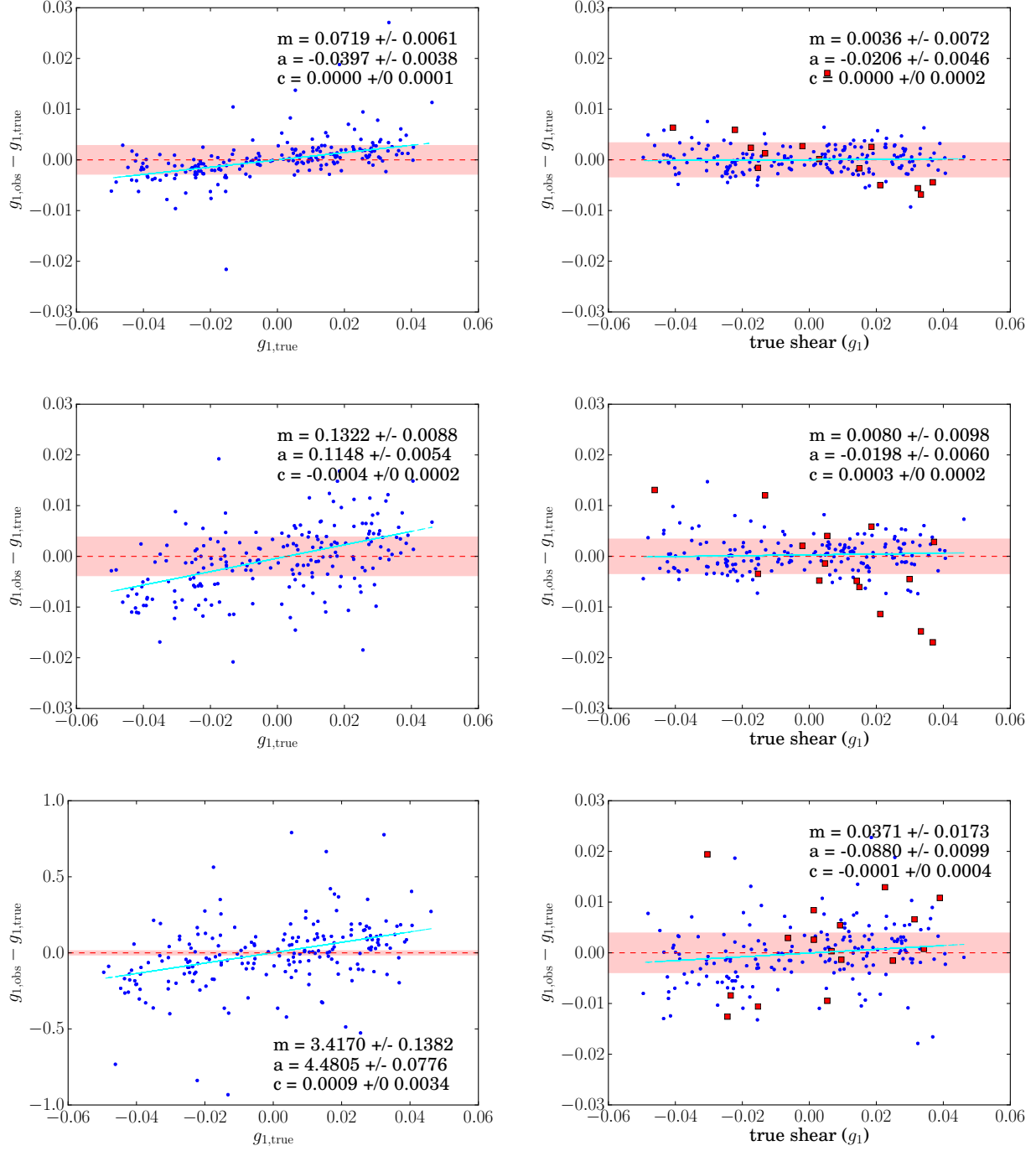


Figure 2. Shear calibration bias m_1 before (left) and after right metacalibration for the regaussianization (top), KSB (middle), and Linear Moments (bottom) algorithms on the CGC branch. The shaded region covers the same vertical range in each panel. Points excluded by the log-likelihood cut are marked with red squares.

Finally, our shear inference procedure is designed to extract the mean shear from a constant-shear field. While this procedure may be applicable to galaxy-galaxy lensing (i.e., projecting the shapes onto the tangent to the appropriate lens), it is not suitable for measurements like cosmic shear that typically rely on second or higher moments of the shear field. While a similar histogram estimation procedure could be implemented to model the responsivity of the distribution of ellipticity products (as

would be needed for two-point shear correlation functions), we leave design and implementation of this generalization to for future work.

At the time of this writing, metacalibration is being actively adapted to realistic measurements in the Dark Energy Survey. Follow-up work (Sheldon et al. 2016) will demonstrate algorithmic improvements that allow this technique to be used on Dark Energy Survey data with state-of-the-art shear estimation algorithms.

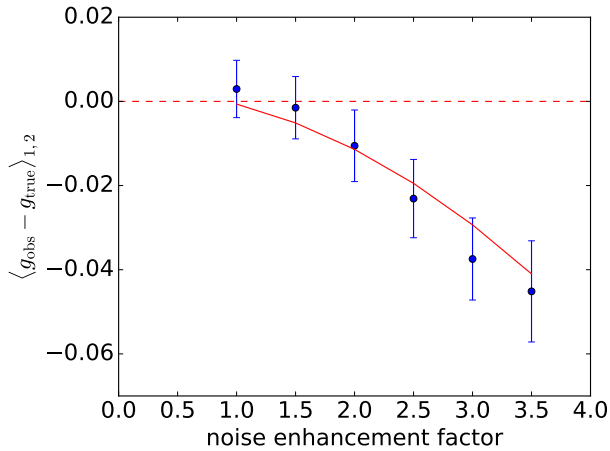


Figure 3. Effects of introducing additional noise. Points with errors correspond to multiplicative shear calibration bias in the control-ground-constant branch when additional noise is added. The noise enhancement factor corresponds to the factor by which the noise in each galaxy image is increased relative to the fiducial GREAT3 simulations. The solid red line shows the expected power-law scaling resulting from correlated noise bias, with a normalization fixed to the measured calibration biases.

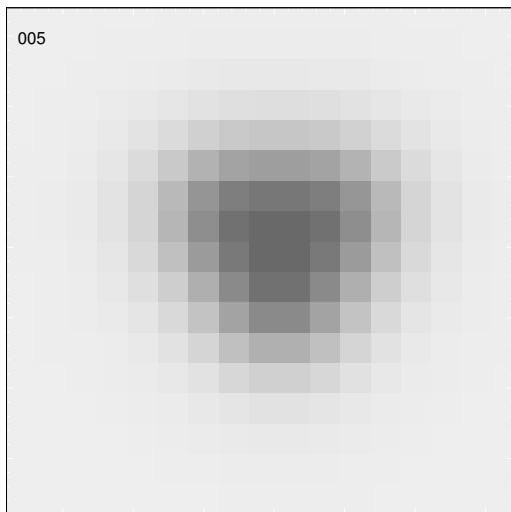


Figure 4. Example of a PSF in one of the simulations with fixed, large aberrations. The most obvious feature in this case is the trefoil, which gives rise to the triangular shape.

7. CONCLUSIONS

We have proposed and implemented the first method for self-calibration of shear measurements that does not rely on external data or simulations for shear calibration. Our method can be wrapped around any sufficiently well-behaved shape measurement algorithm. We use GREAT3 and related simulations to demonstrate that metacalibration reduces or eliminates shear calibration biases across a variety of galaxy morphologies, PSF properties, and for several otherwise biased shape measurement algorithms. We have argued that our technique works because it takes advantage of the fundamental linearity of astronomical images in the shear signal, most astronomical imaging, in combination with the fact that the effects of shear on an image with a known PSF are

model-independent.

Those cases we have examined where the initial biases are large or not linear are not completely corrected by our linear detrending scheme, though in every case we have studied the algorithm appears to substantially improve biases resulting from faulty PSF correction and shear miscalibration. Even the nearly information-free linear moments algorithm appears to be calibrated by our procedure to a level superior to uncorrected KSB, a widely used traditional shear estimation algorithm.

We expect future work to extend this method to deal with the complexities inherent in real data.

REFERENCES

- Bartelmann, M. & Schneider, P. 2001, *Phys. Rep.*, 340, 291
 Bergé, J., Gamper, L., Réfrégier, A., & Amara, A. 2013, *Astronomy and Computing*, 1, 23
 Bernstein, G. M. & Armstrong, R. 2014, *MNRAS*, 438, 1880
 Bernstein, G. M. & Jarvis, M. 2002, *AJ*, 123, 583
 Bridle, S., Shave-Taylor, J., Amara, A., Applegate, D., Balan, S. T., Berge, J., Bernstein, G., Dahle, H., Erben, T., & et al. 2009, *Annals of Applied Statistics*, 3, 6
 de Jong, J. T. A., Verdoes Kleijn, G. A., Boxhoorn, D. R., Buddelmeijer, H., Capaccioli, M., Getman, F., Grado, A., Helmich, E., Huang, Z., Irisarri, N., Kuijken, K., La Barbera, F., McFarland, J. P., Napolitano, N. R., Radovich, M., Sikkema, G., Valentijn, E. A., Begeman, K. G., Brescia, M., Cavuoti, S., Choi, A., Cordes, O.-M., Covone, G., Dall’Ora, M., Hildebrandt, H., Longo, G., Nakajima, R., Paolillo, M., Puddu, E., Rifatto, A., Tortora, C., van Uitert, E., Buddendiek, A., Harnois-Déraps, J., Erben, T., Eriksen, M. B., Heymans, C., Hoekstra, H., Joachimi, B., Kitching, T. D., Klaes, D., Koopmans, L. V. E., Köhlinger, F., Roy, N., Sifón, C., Schneider, P., Sutherland, W. J., Viola, M., & Vriend, W.-J. 2015, *A&A*, 582, A62
 Fenech Conti, I., Herbonnet, R., Hoekstra, H., Merten, J., Miller, L., & Viola, M. 2016, *ArXiv e-prints*
 Flaugher, B. 2005, *International Journal of Modern Physics A*, 20, 3121
 Heymans, C., Van Waerbeke, L., Bacon, D., Berge, J., Bernstein, G., Bertin, E., Bridle, S., & et al. 2006, *MNRAS*, 368, 1323
 Hildebrandt, H., Viola, M., Heymans, C., Joudaki, S., Kuijken, K., Blake, C., Erben, T., Joachimi, B., Klaes, D., Miller, L., Morrison, C. B., Nakajima, R., Verdoes Kleijn, G., Amon, A., Choi, A., Covone, G., de Jong, J. T. A., Dvornik, A., Fenech Conti, I., Grado, A., Harnois-Déraps, J., Herbonnet, R., Hoekstra, H., Köhlinger, F., McFarland, J., Mead, A., Merten, J., Napolitano, N., Peacock, J. A., Radovich, M., Schneider, P., Simon, P., Valentijn, E. A., van den Busch, J. L., van Uitert, E., & Van Waerbeke, L. 2016, *ArXiv e-prints*
 Hirata, C. & Seljak, U. 2003, *MNRAS*, 343, 459
 Hoekstra, H. & Jain, B. 2008, *Annual Review of Nuclear and Particle Science*, 58, 99

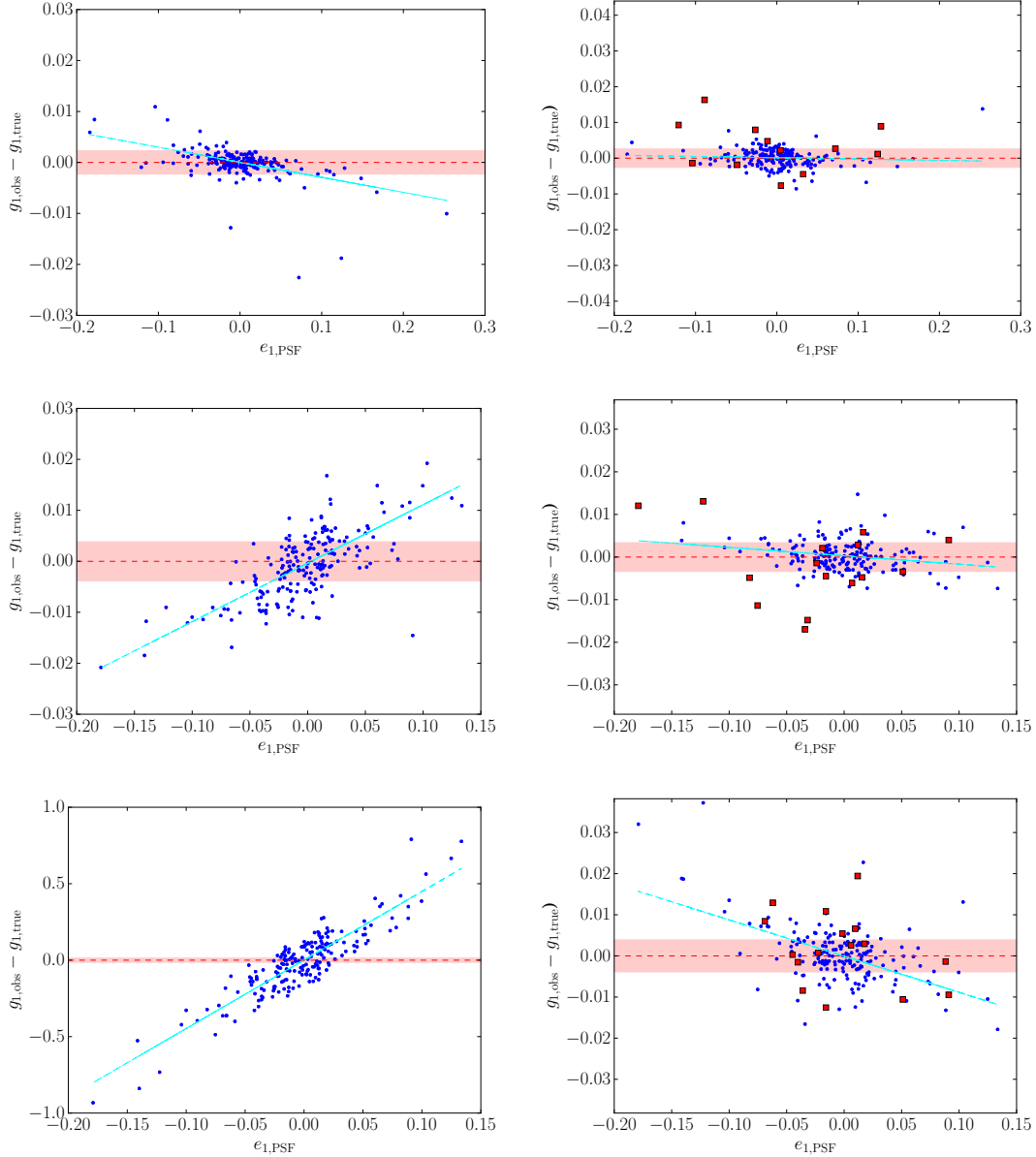


Figure 5. Effects of the metacalibration algorithm applied to PSF correction. **Left** panels show the relationship between measured shear and PSF ellipticity before correction, and **right** panels show the same trends afterwards. Note that the shaded horizontal band covers the same vertical range in each panel.

Simulation branch/algorithm pairs shown in order from **top** to **bottom** are RGC-regauss, CGC-KSB, and CGC-moments. The combination of the metacalibration algorithm with our maximum-likelihood averaging procedure makes accurate corrections when the PSF ellipticities are small or comparable to the magnitude of the shear signal. It is clear that a large fraction of the trend remaining after correction is driven by high-PSF-ellipticity outlier fields, which would typically not pass the image quality requirements in a realistic experiment.

Jarvis, M., Sheldon, E., Zuntz, J., Kacprzak, T., Bridle, S. L., Amara, A., Armstrong, R., Becker, M. R., Bernstein, G. M., Bonnett, C., Chang, C., Das, R., Dietrich, J. P., Drlica-Wagner, A., Eifer, T. F., Gangkofner, C., Gruen, D., Hirsch, M., Huff, E. M., Jain, B., Kent, S., Kirk, D., MacCrann, N., Melchior, P., Plazas, A. A., Refregier, A., Rowe, B., Rykoff, E. S., Samuroff, S., Sánchez, C., Suchyta, E., Troxel, M. A., Vikram, V., Abbott, T., Abdalla, F. B., Allam, S., Annis, J., Benoit-Lévy, A., Bertin, E., Brooks, D., Buckley-Geer, E., Burke, D. L., Capozzi, D., Rosell, A. C., Kind, M. C., Carretero, J., Castander, F. J., Clampitt, J., Crocce, M., Cunha, C. E., D'Andrea, C. B., da Costa, L. N., DePoy, D. L., Desai, S., Diehl, H. T., Doel, P., Neto, A. F., Flaugher, B., Fosalba, P., Frieman, J., Gaztanaga, E., Gerdes, D. W., Gruendl, R. A., Gutierrez, G., Honscheid, K., James, D. J., Kuehn, K., Kuropatkin, N., Lahav, O., Li, T. S., Lima, M., March, M., Martini, P., Miquel, R., Mohr, J. J., Neilsen, E., Nord, B., Ogando, R., Reil, K., Romer, A. K., Roodman, A., Sako, M., Sanchez, E., Scarpine, V., Schubnell, M., Sevilla-Noarbe, I., Smith, R. C., Soares-Santos, M., Sobreira, F., Swanson, M. E. C., Tarle, G., Thaler, J., Thomas, D., Walker, A. B., & Weinberg, S. H. 2016, MNRAS

Kaiser, N. 2000, ApJ, 537, 555
 Kaiser, N., Squires, G., & Broadhurst, T. 1995, ApJ, 449, 460
 Kitching, T. D., Rowe, B., Gill, M., Heymans, C., Massey, R., Witherick, D., Courbin, F., Georgatzis, K., Gentile, M., Gruen, D., Kilbinger, M., Li, G. L., Mariglis, A. P., Meylan, G., Storkey, A., & Xin, B. 2013, ApJS, 205, 12
 Koekemoer, A. M., Aussel, H., Calzetti, D., Capak, P., Giavalisco, M., Kneib, J., Leauthaud, A., Le Fèvre, O., & et al. 2007, ApJS, 172, 196
 Laureijs, R., Amiaux, J., Arduini, S., Auguères, J., Brinchmann, J., Cole, R., Cropper, M., Dabin, C., Duvet, L., Ealet, A., & et al. 2011, ArXiv e-prints (1110.3193)
 LSST Science Collaborations & LSST Project. 2009, ArXiv e-prints (0912.0201), <http://www.lsst.org/lsst/scibook>

branch	algorithm	$m_1 \times 1000$	$m_2 \times 1000$	$a_1 \times 1000$	$a_2 \times 1000$	$c_1 \times 1000$	$c_2 \times 1000$
CGC	regauss (MC)	3.6 ± 7.2	2.3 ± 6.4	-20.6 ± 4.6	-19.4 ± 3.6	$0.0 \pm .2$	0.1 ± 0.2
CGC	regauss	71.9 ± 6.1	65.5 ± 4.9	-39.7 ± 3.8	-43.9 ± 2.9	0.0 ± 0.1	0.0 ± 0.1
CGC	ksb (MC)	8.0 ± 9.8	-17.0 ± 8.7	-19.8 ± 6.0	-9.2 ± 5.0	0.3 ± 0.2	-0.2 ± 0.2
CGC	ksb	132.2 ± 8.8	145.5 ± 10.4	114.8 ± 5.4	109.6 ± 6.1	-0.4 ± 0.2	$0.0 \pm .3$
CGC	moments (MC)	37.1 ± 17.3	45.9 ± 18.4	-88.0 ± 9.9	-87.7 ± 9.5	0.1 ± 0.4	-0.2 ± 0.5
CGC	moments	3417.0 ± 138.2	3223.8 ± 173.1	4480.5 ± 77.6	4604.4 ± 88.8	0.9 ± 3.4	-0.8 ± 4.6
RGC	regauss (MC)	-5.3 ± 7.8	6.1 ± 6.6	3.6 ± 4.0	-3.1 ± 3.7	0.1 ± 0.2	0.1 ± 0.2
RGC	regauss	30.4 ± 5.2	24.9 ± 5.0	-29.5 ± 2.8	-18.6 ± 2.8	0.0 ± 0.1	0.2 ± 0.1
CGC-Noaber	regauss (MC)	-7.4 ± 6.9	6.1 ± 6.4	-33.9 ± 12.7	-23.7 ± 11.2	0.1 ± 0.2	0.1 ± 0.2
CGC-Noaber	regauss	40.7 ± 2.9	-43.9 ± 2.9	-27.4 ± 5.2	-26.5 ± 5.0	0.1 ± 0.1	0.1 ± 0.1
RGC-Noaber	regauss (MC)	7.5 ± 5.0	14.0 ± 4.8	-18.8 ± 9.6	-10.8 ± 9.1	0.0 ± 0.1	0.0 ± 0.1
RGC-Noaber	regauss	16.4 ± 3.0	17.4 ± 3.4	2.2 ± 5.8	2.5 ± 6.4	0.2 ± 0.1	0.0 ± 0.1
RGC-FixedAber	regauss (MC)	-4.7 ± 8.9	6.0 ± 7.2	-15.4 ± 22.1	-16.0 ± 17.5	0.1 ± 0.2	-0.2 ± 0.2
RGC-FixedAber	regauss	61.6 ± 6.6	63.7 ± 5.2	-30.0 ± 12.1	-32.3 ± 13.5	0.3 ± 0.2	0.0 ± 0.1

Figure 6. Shear and PSF calibration bias parameters from each of the branches considered. Rows with metacalibrated parameters are shown above their un-calibrated counterparts.

- Mandelbaum, R., Hirata, C. M., Leauthaud, A., Massey, R. J., & Rhodes, J. 2012, MNRAS, 420, 1518
- Mandelbaum, R., Hirata, C. M., Seljak, U., Guzik, J., Padmanabhan, N., Blake, C., Blanton, M. R., Lupton, R., & Brinkmann, J. 2005, MNRAS, 361, 1287
- Mandelbaum, R., Rowe, B., Armstrong, R., Bard, D., Bertin, E., Bosch, J., Boutigny, D., Courbin, F., Dawson, W. A., Donnarumma, A., Fenech Conti, I., Gavazzi, R., Gentile, M., Gill, M. S. S., Hogg, D. W., Huff, E. M., Jee, M. J., Kacprzak, T., Kilbinger, M., Kuntzer, T., Lang, D., Luo, W., March, M. C., Marshall, P. J., Meyers, J. E., Miller, L., Miyatake, H., Nakajima, R., Ngolé Mboula, F. M., Nurbaeva, G., Okura, Y., Paulin-Henriksson, S., Rhodes, J., Schneider, M. D., Shan, H., Sheldon, E. S., Simet, M., Starck, J.-L., Sureau, F., Tewes, M., Zarb Adami, K., Zhang, J., & Zuntz, J. 2015, MNRAS, 450, 2963
- Mandelbaum, R., Rowe, B., Bosch, J., Chang, C., Courbin, F., Gill, M., Jarvis, M., Kannawadi, A., Kacprzak, T., Lackner, C., & et al. 2014, ApJS, 212, 5
- Mandelbaum, R., Slosar, A., Baldauf, T., Seljak, U., Hirata, C. M., Nakajima, R., Reyes, R., & Smith, R. E. 2013, MNRAS, 432, 1544
- Massey, R., Heymans, C., Bergé, J., Bernstein, G., Bridle, S., Clowe, D., Dahle, H., Ellis, R., & et al. 2007a, MNRAS, 376, 13
- Massey, R., Kitching, T., & Richard, J. 2010, Reports on Progress in Physics, 73, 086901
- Massey, R., Rowe, B., Refregier, A., Bacon, D. J., & Bergé, J. 2007b, MNRAS, 380, 229
- Miyazaki, S., Komiyama, Y., Nakaya, H., Kamata, Y., Doi, Y., Hamana, T., Karoji, H., Furusawa, H., Kawanomoto, S., Morokuma, T., Ishizuka, Y., Nariai, K., Tanaka, Y., Uraguchi, F., Utsumi, Y., Obuchi, Y., Okura, Y., Oguri, M., Takata, T., Tomono, D., Kurakami, T., Namikawa, K., Usuda, T., Yamanoi, H., Terai, T., Uekiyo, H., Yamada, Y., Koike, M., Aihara, H., Fujimori, Y., Mineo, S., Miyatake, H., Yasuda, N., Nishizawa, J., Saito, T., Tanaka, M., Uchida, T., Katayama, N., Wang, S.-Y., Chen, H.-Y., Lupton, R., Loomis, C., Bickerton, S., Price, P., Gunn, J., Suzuki, H., Miyazaki, Y., Muramatsu, M., Yamamoto, K., Endo, M., Ezaki, Y., Itoh, N., Miwa, Y., Yokota, H., Matsuda, T., Ebinuma, R., & Takeshi, K. 2012, in Proc. SPIE, Vol. 8446, Ground-based and Airborne Instrumentation for Astronomy IV, 84460Z
- Refregier, A. 2003, ARA&A, 41, 645
- Rowe, B. T. P., Jarvis, M., Mandelbaum, R., Bernstein, G. M., Bosch, J., Simet, M., Meyers, J. E., Kacprzak, T., Nakajima, R., Zuntz, J., Miyatake, H., Dietrich, J. P., Armstrong, R., Melchior, P., & Gill, M. S. S. 2015, Astronomy and Computing, 10, 121
- Schneider, P. 2006, in Saas-Fee Advanced Course 33: Gravitational Lensing: Strong, Weak and Micro, ed. G. Meylan, P. Jetzer, P. North, P. Schneider, C. S. Kochanek, & J. Wambsganss, 269–451
- Scoville, N., Abraham, R. G., Aussel, H., Barnes, J. E., Benson, A., Blain, A. W., Calzetti, D., Comastri, A., Capak, P., & et al. 2007a, ApJS, 172, 38
- Scoville, N., Aussel, H., Brusa, M., Capak, P., Carollo, C. M., Elvis, M., Giallisco, M., Guzzo, L., Hasinger, G., & et al. 2007b, ApJS, 172, 1
- Spergel, D., Gehrels, N., Baltay, C., Bennett, D., Breckinridge, J., Donahue, M., Dressler, A., Gaudi, B. S., Greene, T., Guyon, O., Hirata, C., Kalirai, J., Kasdin, N. J., Macintosh, B., Moos, W., Perlmutter, S., Postman, M., Rauscher, B., Rhodes, J., Wang, Y., Weinberg, D., Benford, D., Hudson, M., Jeong, W.-S., Mellier, Y., Traub, W., Yamada, T., Capak, P., Colbert, J., Masters, D., Penny, M., Savransky, D., Stern, D., Zimmerman, N., Barry, R., Bartusek, L., Carpenter, K., Cheng, E., Content, D., Dekens, F., Demers, R., Grady, K., Jackson, C., Kuan, G., Kruk, J., Melton, M., Nemati, B., Parvin, B., Poberezhskiy, I., Peddie, C., Ruffa, J., Wallace, J. K., Whipple, A., Wollack, E., & Zhao, F. 2015, ArXiv e-prints
- Weinberg, D. H., Mortonson, M. J., Eisenstein, D. J., Hirata, C., Riess, A. G., & Rozo, E. 2013, Phys. Rep., 530, 87
- Zhang, J. & Komatsu, E. 2011, MNRAS, 414, 1047

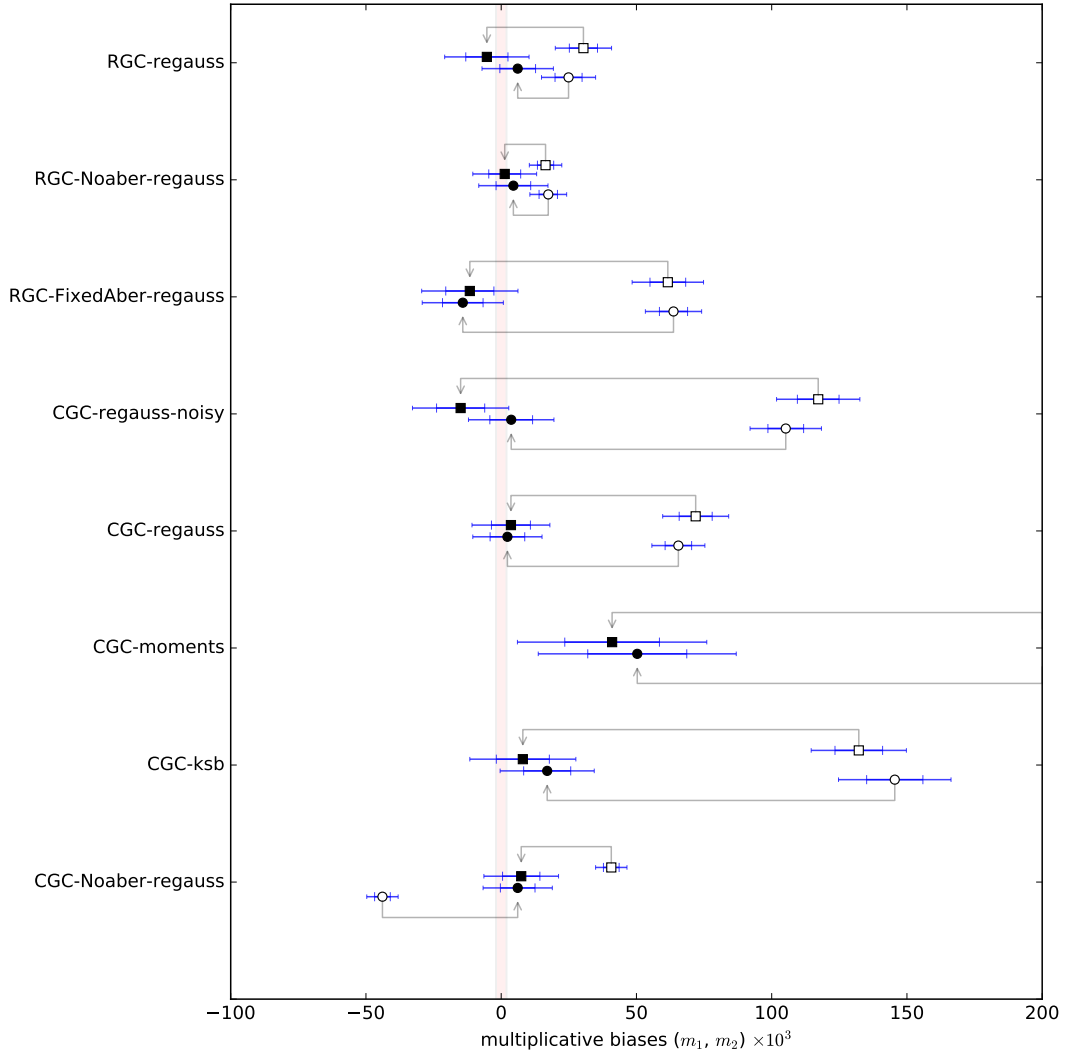


Figure 7. Calibration bias results. Each row shows multiplicative calibration bias m_1 (top) and m_2 (bottom) before and after metacalibration. Pre- and post-correction points are connected by gray arrows: in every case the procedure has reduced or eliminated the amplitude of detectable multiplicative calibration bias.

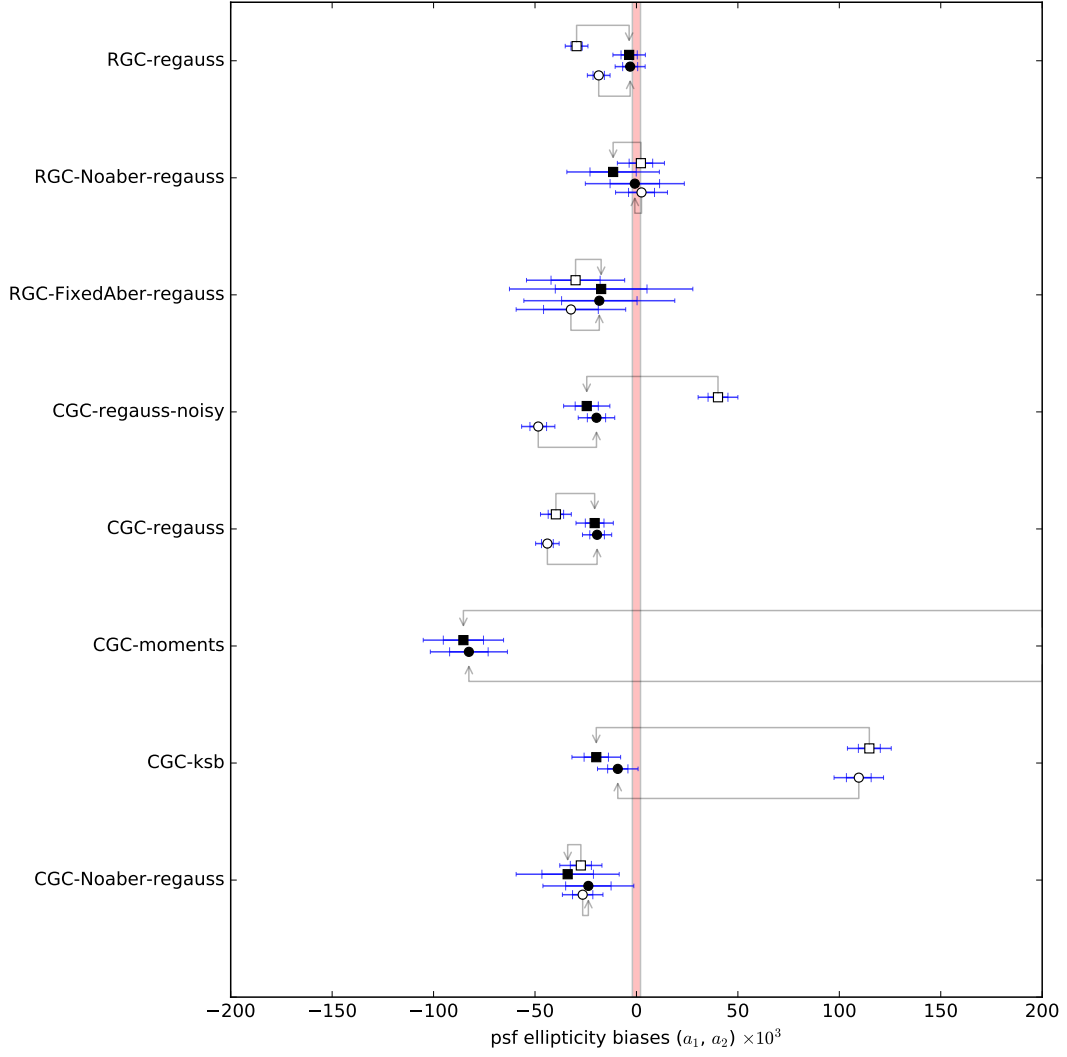


Figure 8. Calibration bias results. Each row shows linear coupling between the PSF ellipticity and the measured shape a_1 (top) and a_2 (bottom) before and after metacalibration. Pre- and post-correction points are connected by gray arrows: in every case the procedure has reduced or eliminated the amplitude of detectable PSF coupling.